Inorg. Chem. **2008**, *47*, 9216−9227

Computational Studies of the Reactions of $B_{10}H_{13}^-$ with Alkynes and Olefins: Pathways for Dehydrogenative Alkyne-Insertion and Olefin-Hydroboration Reactions

Chang Won Yoon, Upal Kusari, and Larry G. Sneddon*

Department of Chemistry, University of Pennsylvania, Philadelphia, Pennsylvania 19104-6323

Received May 31, 2008

Quantum mechanical computational studies of possible mechanistic pathways for $B_{10}H_{13}^-$ dehydrogenative alkyne-insertion and olefin-hydroboration reactions demonstrate that, depending on the reactant and reaction conditions, $B_{10}H_{13}^-$ can function as either an electrophile or nucleophile. For reactions with nucleophilic alkynes, such as propyne, the calculations indicate that at the temperatures (∼110−120 °C) required for these reactions, the ground-state $B_{10}H_{13}^-$ (**1**) structure can rearrange to an electrophilic-type cage structure **3** having a LUMO orbital strongly localized on the B6 cage-boron. Alkyne binding at this site followed by subsequent steps involving the formation of additional boron−carbon bonds, hydrogen elimination, protonation, and further hydrogen elimination then lead in a straightforward manner to the experimentally observed *ortho*-carborane products resulting from alkyne insertion into the decaborane framework. A similar mechanistic sequence was identified for the reaction of propyne with 6-R-$B_{10}H_{12}^-$ leading to the formation of 1-Me-3-R-1,2-$C_2B_{10}H_{11}$ carboranes. On the other hand, both $B_{10}H_{13}^-$ and 4,6-$C_2B_7H_{12}^-$ have previously been shown to react at much lower temperatures with strongly polarized alkynes, and the DFT and IRC calculations support an alternative mechanism involving initial nucleophilic attack by these polyborane anions at the positive terminal acetylenic carbon to produce terminally substituted olefinic anions. In the case of the $B_{10}H_{13}^-$ reaction, subsequent cyclization steps were identified that provide a pathway to the experimentally observed *arachno*-8-(NC)-7,8-$C_2B_{10}H_{14}^-$ carborane. The computational study of $B_{10}H_{13}^-$ propylene hydroboration also supports a mechanistic pathway involving a cage rearrangement to the electrophilic **3** structure. Olefin-binding at the LUMO orbital localized on the B6 cage-boron, followed by addition of the B6−H group across the olefinic double bond and protonation, then leads to the experimentally observed 6-R-$B_{10}H_{13}$ products.

Introduction

The preceding two papers in this series demonstrated that ionic liquids promote both decaborane dehydrogenative alkyne-insertion reactions[1] to give *ortho*-carboranes and decaborane olefin-hydroboration reactions[2] to give 6-R-$B_{10}H_{13}$-substituted decaboranes. In both cases, the experimental evidence indicated that the $B_{10}H_{13}^-$ anion was the key initial reactant. In this paper, we present DFT and IRC computational studies of the structure and reactivities of $B_{10}H_{13}^-$, along with possible mechanistic pathways for the $B_{10}H_{13}^-$ dehydrogenative alkyne-insertion and olefin-hydroboration reactions. The results demonstrate that, depending on the reactant and reaction conditions, $B_{10}H_{13}^-$ can function as either an electrophile or nucleophile.

Computational Methods

Hartree−Fock (HF), density functional theory (DFT), and second-order Møller−Plesset perturbation theory (MP2) calculations were performed using the Gaussian 03 package.[3] All ground-state, transition-state, and intermediate geometries along the reaction pathways were fully optimized consecutively at HF/6−31G(d) and B3LYP/6−31+G(d,p) levels without any symmetry constraints. Harmonic vibrational analyses were carried out on the optimized geometries at the same level to establish the nature of stationary points. True first-order saddle points possessed only one imaginary frequency. Intrinsic reaction coordinate (IRC) calculations were carried out in both the forward and reverse directions to confirm the reaction pathways from the located transition states. All MP2

* To whom correspondence should be addressed. E-mail: lsneddon@sas.upenn.edu.

(1) Li, Y.; Carroll, P. J.; Sneddon, L. G. *Inorg. Chem.* **2008**, *47*, 9193–9202.

(2) Kusari, U.; Carroll, P. J.; Sneddon, L. G. *Inorg. Chem.* **2008**, *47*, 9203–9215.

10.1021/ic8010019 CCC: $40.75
Published on Web 09/19/2008

energies (Table 1) were computed on the DFT-optimized geometries using a frozen core approximation (i.e., only valence electrons were considered for the electron correlation treatment) in conjunction with 6−311+G(d,p) basis set. The zero-point vibrational energies were computed at the B3LYP/6−31+G(d,p) level and then scaled.[4] All reported MP2 energies are corrected using the scaled zero point energies. The MP2 calculated energies are given in the figures. Dashed lines between any two intermediates in the figures indicate that a transition state was confirmed between these intermediates by a HF/IRC calculation, but that the MP2 calculated energy of the DFT-optimized transition state dropped below one of the intermediates.[5] The calculated electronic and Gibbs free energies at 393.15 K for all reactions at the B3LYP/6−31+G(d,p) level are also listed in Table S1, Supporting Information.

Results and Discussion

Geometric and Electronic Structures of the $B_{10}H_{13}^-$ and 6-R-$B_{10}H_{12}^-$ Anions. Decaborane, $B_{10}H_{14}$, is a monoprotic Brønsted acid that is readily deprotonated by bases such as triethylamine to form the $B_{10}H_{13}^-$ anion.[6]

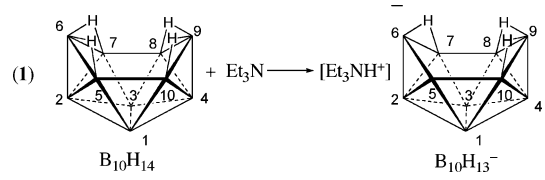

X-ray crystallographic studies of the $[Et_3NH^+][B_{10}H_{13}^-]$[7] and $[PhCH_2NMe_3^+][B_{10}H_{13}^-]$[8] salts have established that in the solid state, the anion has the C_1-symmetric structure (**1**) indicated in eq 1 and Figure 1 resulting from the loss of one bridging hydrogen. However, the solution 70.6 MHz ^{11}B NMR spectrum of $B_{10}H_{13}^-$ was reported to show only four resonances in 2:1:5:2 ratios suggesting the C_s-symmetric structure **2** that is also shown in Figure 1.[9] This apparent conflict was resolved by Hofmann and Schleyer's computational studies,[10] which showed that at the MP2/6−31G(d) level, the C_1 structure is, in fact, 4.5 kcal/mol lower in energy than the C_s structure (**2**) and that the C_s symmetric pattern observed in the NMR can be explained by a fluxional hydrogen rearrangement that interconverts the two enantiomeric forms of the anion. Averaging the calculated chemical shifts for the B6−B9, B5−B10, B7−B8, and B2−B4 pairs of boron atoms that are affected by the fluxional process then gives excellent agreement with the experimentally observed spectrum.

Hawthorne has previously shown[6] that, even though it is negatively charged, $B_{10}H_{13}^-$ can function as an electrophile and form adducts with bases such as amines and phosphines (eq 2).

$$B_{10}H_{13}^- + R3E \rightarrow 6\text{-}R_3E\text{-}B_{10}H_{13}^- \quad E = N \text{ or } P \qquad (2)$$

The Hofmann and Schleyer computational studies[10] yielded the structures shown in Figure 2 for these adducts having the base attached at the endo or exo (lower energy) positions of the B6 boron on a $B_{10}H_{13}^-$ framework (**3**), Figure 1, where the hydrogens are in different locations than those in either the C_1 (**1**) or C_s (**2**) structures.

Thus, at least three different framework arrangements appear possible for $B_{10}H_{13}^-$. As an initial step in developing an understanding of the reactions of $B_{10}H_{13}^-$ with alkynes and olefins, we computationally evaluated the energies and electronic structures of these three types of structures (Figure 1). In agreement with the earlier reported studies, MP2 energy calculations based on the B3LYP/6−31+G(d,p) optimized geometries find that structure **1** is 4.6 kcal/mol lower than **2** and that **3** is also only 20.1 kcal/mol higher than **1**.

The density surface plots for the three structures show very different types of HOMO and LUMO orbitals. For **1**, the LUMO is delocalized over all six atoms on the open face, with only a small component at B6 and B9. The HOMO, consistent with the removal of the proton from the B5−B6 edge, is localized above and below the B5−B6 edge suggesting strong nucleophilic reactivity at this position. For **2**, the HOMO surface density is localized on the B5−B6−B7 and the B8−B9−B10 edges, while the LUMO has its largest components at B6, B9 and the B7−B8 edge. Most interestingly, the HOMO density for **3** is mainly at B9, while the LUMO orbital is highly localized at B6, suggesting high electrophilic character at B6. As pointed out by reviewer 1, the predicted electrophilic character for **3** is consistent with the fact that while $B_{10}H_{13}^-$ has a nido-electron count (24 skeletal electrons), **3** can be viewed as having an arachno type structure (i.e., requiring 26 skeletal electrons) derived by removal of one endo-hydride from the *arachno*-$B_{10}H_{14}^{2-}$ structure.[10,11] The isoelectronic *nido*-SB_9H_{11} thiaborane cluster has likewise been shown to have strong electrophilic

(3) Frisch, M. J.; Trucks, G. W.; Schlegel, H. B.; Scuseria, G. E.; Robb, M. A.; Cheeseman, J. R.; Montgomery, J. A., Jr.; Vreven, T; Kudin, K. N.; Burant, J. C.; Millam, J. M.; Iyengar, S. S.; Tomasi, J.; Barone, V.; Mennucci, B.; Cossi, M.; Scalmani, G.; Rega, N.; Petersson, G. A.; Nakatsuji, H.; Hada, M.; Ehara, M.; Toyota, K.; Fukuda, R.; Hasegawa, J.; Ishida, M.; Nakajima, T.; Honda, Y.; Kitao, O.; Nakai, H.; Klene, M.; Li, X.; Knox, J. E.; Hratchian, H. P.; Cross, J. B.; Adamo, C.; Jaramillo, J.; Gomperts, R.; Stratmann, R. E.; Yazyev, O.; Austin, A. J.; Cammi, R.; Pomelli, C.; Ochterski, J. W.; Ayala, P. Y.; Morokuma, K.; Voth, G. A.; Salvador, P.; Dannenberg, J. J.; Zakrzewski, V. G.; Dapprich, S.; Daniels, A. D.; Strain, M. C.; Farkas, O.; Malick, D. K.; Rabuck, A. D.; Raghavachari, K.; Foresman, J. B.; Ortiz, J. V.; Cui, Q.; Baboul, A. G.; Clifford, S.; Cioslowski, J.; Stefanov, B. B.; Liu, G.; Liashenko, A.; Piskorz, P.; Komaromi, I.; Martin, R. L.; Fox, D. J.; Keith, T.; Al-Laham, M. A.; Peng, C. Y.; Nanayakkara, A.; Challacombe, M.; Gill, P. M. W.; Johnson, B.; Chen, W.; Wong, M. W.; Gonzalez, C.; Pople, J. A. *Gaussian 03*, revision B.05; Gaussian, Inc.: Pittsburgh PA, 2003.
(4) Merrick, J. P.; Moran, D.; Radom, L. *J. Phys. Chem. A* **2007**, *111*, 11683–11700.
(5) Small computed energy inversions between confirmed transition-states and intermediates on relatively flat potential energy surfaces are not uncommon when using different computational methods, for example, see: (a) Figure 2 in Domingo, L. R.; Oliva, M.; Andres, J. *J. Org. Chem.* **2001**, *66*, 6151–6157. (b) Figure 7b in Wu, R.; McMahon, T. B. *J. Am. Chem. Soc.* **2008**, *130*, 3065–3078. (c) Figure 4 in Sayin, H.; McKee, M. L. *Inorg. Chem.* **2007**, *46*, 2883–2891.
(6) Graybill, B. M.; Pitochelli, A. R.; Hawthorne, M. F. *Inorg. Chem.* **1962**, *1*, 622–626.
(7) Sneddon, L. G.; Huffman, J. C.; Schaeffer, R. O.; Streib, W. E. *Chem. Commun.* **1972**, *8*, 474–5.
(8) Wynd, A. J.; Welch, A. J. *Acta Crystallogr.* **1989**, *C45*, 615–617.
(9) Siedle, A. R.; Bodner, G. M.; Todd, L. J. *J. Inorg. Nucl. Chem.* **1971**, *33*, 3671–3676.
(10) Hofmann, M.; Schleyer, P. v. R. *Inorg. Chem.* **1998**, *37*, 5557–5565.
(11) McKee, M. L. *Inorg. Chem.* **1994**, *33*, 6213–6218.

Table 1. Calculated MP2 Energies for the Reactions of $B_{10}H_{13}^-$, 6-(C_3H_7)-$B_{10}H_{12}^-$, and 4,6-$C_2B_7H_{12}^-$

reactions

1 → 3 (Figure *3*)

	E (in hartrees)	E_{rel} (kcal/mol)
1	−255.3915466	0.0
TS1	−255.3840662	4.7
2	−255.3841530	4.6
3	−255.3594406	20.1

1-R → 1′-R, **3-R**, and **3′-R** (Figure *5*)

	E (in Hartrees)	E_{rel} (kcal/mol)
1-R	−372.9088677	0.0
TS1-R	−372.9004788	5.3
2-R	−372.9012204	4.8
1′-R	−372.9075360	0.8
3-R	−372.8806502	17.7
3′-R	−372.8741849	21.8

(**A**) **3** + NH_3 (Figure *6*)

	E (in hartrees)	E_{rel} (kcal/mol)
3 + NH_3	−311.7415316	0.0
A-TS2	−311.7370410	2.8
4	−311.7708645	−18.4
5	−311.7754256	−21.3

(**G**) 4,6-$C_2B_7H_{12}^-$ + cyanoacetylene (Figure *12*)

	E (in hartrees)	E_{rel} (kcal/mol)
$C_2B_7H_{12}^-$ + cyanoacetylene	−425.5930889	0.0
G-TS1	−425.5912448	1.2
G-Int1	−425.6627616	−43.7
G-TS2	−425.6536325	−38.0
13	−425.6683034	−47.2

(**B**) **3-R** + NH_3 (Figure *7*)

	E (in hartrees)	E_{rel} (kcal/mol)
3-R + NH_3	−429.2627412	0.0
B-TS2	−429.2556802	4.4
6	−429.2878156	−15.7
7	−429.2848111	−13.8

(**C**) **3′-R** + NH_3 (Figure *7*)

	E (in hartrees)	E_{rel} (kcal/mol)
3′-R + NH_3	−429.2562759	0.0
C-TS2	−429.2527797	2.2
8	−429.2864191	−18.9
9	−429.2916256	−22.2

(**D**) **3** + Propyne (Figure *9*)

	E (in hartrees)	E_{rel} (kcal/mol)
3 + propyne	−371.6223350	0.0
D-TS2	−371.6133201	5.7
D-Int3	−371.6486701	−16.5
D-Int3′	−371.6463949	−15.1
D-TS3	−371.6479752	−16.1
D-Int4	−371.6787696	−35.4
D-TS4	−371.6544401	−20.1
D-Int5	−371.7035887	−51.0
D-Int5 + NEt_3H^+	−663.4337035	0.0
D-Int6 + NEt_3 + H_2	−663.5867329	−96.0
D-Int6	−371.0777086	0.0
D-TS5	−371.0682166	6.0
10 + H_2	−370.1695922	−57.7

(**E**) **3-R** + Propyne (Figure *10*)

	E (in hartrees)	E_{rel} (kcal/mol)
3-R + propyne	−489.1435446	0.0
E-TS2	−489.1324364	7.0
E-Int3	−489.2028609	−37.2
E-TS3	−489.1756619	−20.2
E-Int4	−489.2140404	−44.2
E-Int4 + NEt_3H^+	−780.9441553	0.0
E-Int5 + NEt_3 + H_2	−781.1078138	−102.7
E-Int5	−488.5987895	0.0
E-TS5	−488.5892422	6.0
11 + H_2	−488.6903507	−57.5

(**F**) **1** + Cyanoacetylene (Figure *11*)

	E (in hartrees)	E_{rel} (kcal/mol)		*E* (in hartrees)	E_{rel} (kcal/mol)
1 + cyanoacetylene	−424.5128541	0.0	**F-TS3**	−424.5578541	−28.2
F-TS1	−424.5059099	4.4	**F-Int3**	−424.5690308	−35.3
F-Int1	−424.5211396	−5.2	**F-TS4**	−424.5686479	−35.0
F-TS2	−424.5119425	0.6	**12**	−424.6312788	−74.3
F-Int2	−424.5859070	−45.8			

(**H**) **3** + propylene (endo-hydroboration) (Figure *14*)

	E (in hartrees)	E_{rel} (kcal/mol)
3 + propylene	−372.8288465	0.0
H-TS2	−372.8228883	3.7
H-Int3	−372.8595897	−19.3
H-TS3	−372.8279171	0.6
H-Int4 (2-R)	−372.9012204	−45.4
H-TS4	−372.9004788	−44.9
14 (1-R)	−372.9088677	−50.2

(**H**) **3** + propylene (exo-hydroboration) (Figure *15*)

	E (in hartrees)	E_{rel} (kcal/mol)
3 + propylene	−372.8288465	0.0
H-Int3′	−372.8669127	−23.9
H-TS2′	−372.8555921	7.1
H-Int4′	−372.8584176	−18.6
H-TS3′	−372.8399135	−6.9
H-Int5′	−372.8806553	−32.5
H-TS4′	−372.8763742	−29.8

properties, including the ability to hydroborate both olefins and acetylenes, as a result of an accepting orbital localized on one facial boron.[12]

Intrinsic reaction coordinate (IRC) calculations support the pathway illustrated in Figure 3 for the conversion of **1** to the higher energy structures **2** (**Int1**) and **3** (**Int2**). As shown in the figure, the relative energies of this pathway were investigated at the (a) HF (6−31G(d)), (b) DFT (B3LYP/6−31+G(d,p)) and (c) MP2 (6−311+G(d,p)) levels. In the initial step, the B9−B10 bridging hydrogen in **1** moves to the endo-B10 position in **TS1**, then continues to the B5−B10 edge to form **2**, with calculated barriers to **TS1** of 7.8 (HF), 5.2 (DFT), and 4.7 kcal/mol (MP2), respectively. The conversion of **2** to **TS2**, which involves the movement of

(12) Meneghelli, B. J.; Canter, B. N.; Rudolph, R. W. *J. Am. Chem. Soc.* **1980**, *102*, 4355–4360.

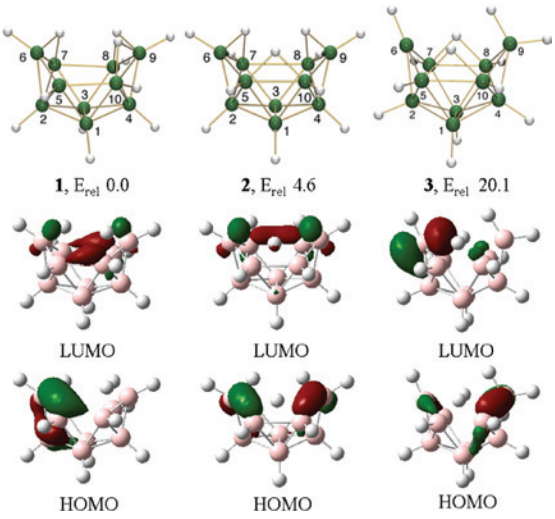

Figure 1. B3LYP/6−31+G(d,p) optimized structures and their HOMO and LUMO density surfaces for $B_{10}H_{13}^-$. The MP2 calculated energies are in kcal/mol.

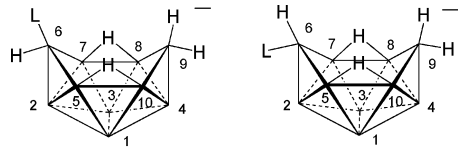

Figure 2. Proposed structures of 6-L-$B_{10}H_{13}^-$ complexes with a **3**-type $B_{10}H_{13}^-$ framework.

bridge-hydrogens to the endo-positions at the B7 and B9 borons, then requires much higher energy 11.7 (HF), 12.7 (DFT) and 14.7 kcal/mol (MP2), respectively. The energy for the conversion of **TS2** to **3** is small and, in fact, the calculated energies of **TS2** and **3** at the DFT and MP2 levels are slightly inverted, reflecting a nearly flat potential energy surface between **TS2** and **3**.[5] The 120 °C free energy diagram (d) for the DFT (B3LYP/6−31+G(d,p)) geometries likewise shows a nearly flat surface between **TS2** and **3**, but in this case with **TS2** at slightly higher energy. The IRC calculations at both the HF and DFT levels also clearly showed connection of **TS2** to both **2** and **3**. Moreover, none of the optimized structures of **3** (including, those at the HF/6−31G(d), B3LYP/6−31+G(d,p), B3LYP/6−311+G(d,p), and B3LYP/6−311+G(2d,p) levels) had imaginary frequencies, thus indicating that **3** (**Int2**) is an intermediate (i.e., not a transition state) on these potential energy surfaces.

As shown in Figure 4, computational studies of the geometric and electronic structures of a 6-R-$B_{10}H_{12}^-$ derivative (R = C_3H_7) also showed that a C_1-symmetric structure was lowest in energy. But, depending upon whether the B5−B6 or B9−B10 bridging-proton of decaborane is removed, two different C_1-symmetric 6-R-$B_{10}H_{12}^-$ structures (i.e., **1-R** and **1′-R**, respectively) result, with the calculations indicating that the **1-R** structure is only slightly more stable (0.8 kcal/mol) than **1′-R**. The fact that they are close in energy suggests that the **1-R** and **1′-R** structures could interconvert in solution. Such an interconversion could occur by either an intermolecular or intramolecular exchange process. DFT and IRC calculations for an intramolecular process yielded the energy profile shown in Figure 5, where

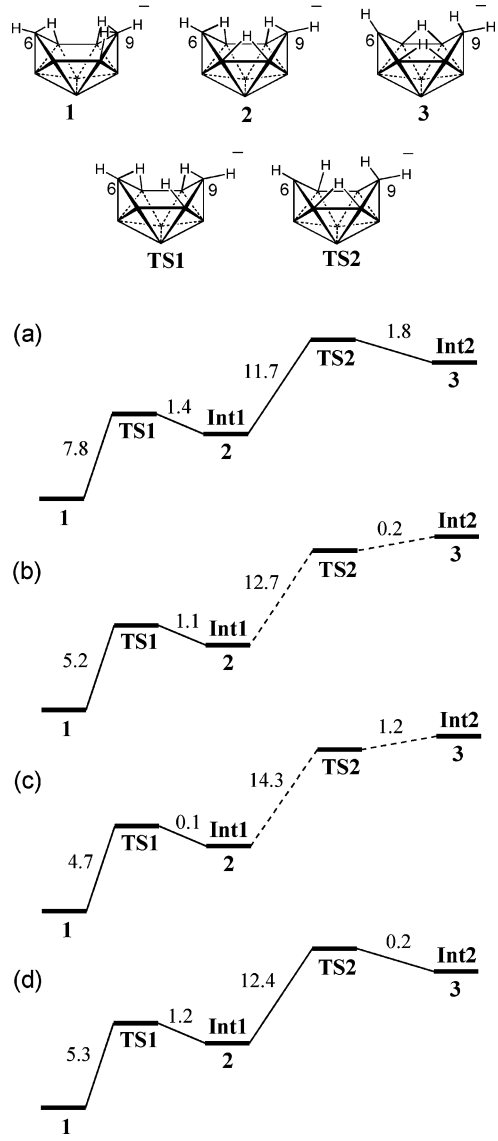

Figure 3. Relative calculated energies (0 K) at the (a) HF (6−31G(d)), (b) DFT (B3LYP/6−31+G(d,p)), and (c) MP2 (6−311+G(d,p) levels and (d) DFT (B3LYP/6−31+G(d,p)) free energies at 393.15 K (from Table S1, Supporting Information) for a pathway for the interconversions of **1**, **2** and **3**. All calculated energies are in kcal/mol.

the initial step is again the conversion of the B9−B10 bridging hydrogen to the endo-B10 position in **TS1-R**, before moving to the B5−B10 edge in **2-R**. The conversion of **2-R** to **1′-R** then involves the rearrangement of the B5−B10 bridging hydrogen to the B5−B6 edge. The 5.3 kcal/mol required to form **TS1-R** (Table 1) is a value nearly identical to the MP2 calculated barrier (5.4 kcal/mol) for the interconversion of the parent $B_{10}H_{13}^-$ enantiomeric (**1**) geometries,[10] further supporting the possibility that **1-R** and **1′-R** interconvert in solution at room temperature.

As was the case for the parent $B_{10}H_{13}^-$ structure **1**, the HOMO densities for **1-R** and **1′-R** are highly localized at the B5−B6 and B9−B10 edges, while their LUMOs are delocalized over the six boron atoms on the open face, with only small components at B6 and B9. Structure **2-R**, which has a similar hydrogen arrangement as the parent **2** structure, was 4.8 kcal/mol less stable than **1-R**, with the HOMO and LUMO orientations being similar to those found for **2**.

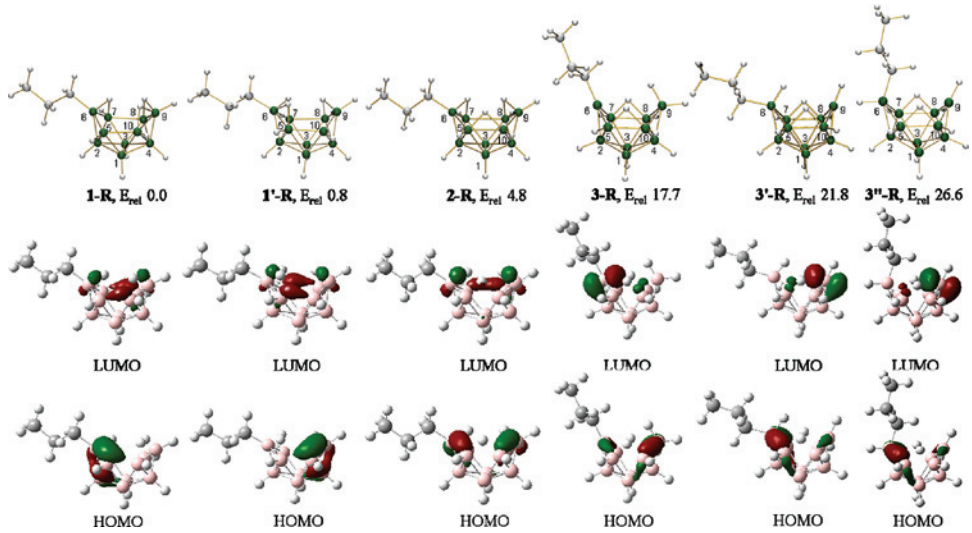

Figure 4. B3LYP/6−31+G(d,p) optimized structures and their HOMO and LUMO density surfaces for 6-C_3H_7-$B_{10}H_{12}^-$. The MP2 calculated energies are in kcal/mol.

The **3-R**, **3′-R**, and **3″-R** structures that are derived from the parent structure **3** were 17.7, 21.8, and 26.6 kcal/mol higher in energy than **1-R**, and the DFT and IRC calculations showed that the lower energy **3-R** and **3′-R** structures can be formed directly from **2-R** as also depicted in Figure 5. The three structures differ from each other by the position of attachment of the R-substituent. In **3-R**, the R is attached to a boron (B6) having no other hydrogen, whereas in **3′-R** and **3″-R** the R-bonded boron (B6) also has another attached hydrogen with the R-group then in either the exo (**3′-R**) or endo (**3″-R**) positions. In all three isomers, the HOMO is centered at the boron with an endo substituent, while the LUMO is located at the boron without the *endo*-hydrogen. The LUMO boron in **3-R** also has an attached *exo*-R group, whereas the R-groups in **3′-R** and **3″-R** are instead attached at the HOMO boron.

Electrophilic Reactions of (A) $B_{10}H_{13}^-$ and (B and C) 6-R-$B_{10}H_{12}^-$ with Lewis Bases. While the Hofmann and Schleyer studies[10] established the structures shown earlier in Figure 2 for the 6-L-$B_{10}H_{13}^-$ base adducts, there was no investigation of the reaction pathway leading from the ground-state structure $B_{10}H_{13}^-$ (**1**) to the observed structures. DFT and IRC studies of possible mechanisms for the $B_{10}H_{13}^-$ reaction (**A**) with ammonia led to the pathway illustrated in Figure 6. The initial step involves the conversion of **1** to **3** by the process shown in Figure 3 that was discussed earlier. Donation of the ammonia nitrogen lone-pair to **3** at the B6 localized LUMO orbital then generates either the 6-*endo*-NH_3-$B_{10}H_{13}^-$ or 6-*exo*-NH_3-$B_{10}H_{13}^-$ isomers. Our calculations indicate, in agreement with the earlier studies,[10] that 6-*exo*-NH_3-$B_{10}H_{13}^-$ is more stable (2.9 kcal/mol) than 6-*endo*-NH_3-$B_{10}H_{13}^-$ and, in addition, that there is a lower kinetic barrier for exo approach. Calculations for the reaction of **3** with CH_3CN also showed that the exo-adducts were both kinetically and thermodynamically favored.

The reaction of 6-(C_3H_7)-$B_{10}H_{12}^-$ with ammonia could in principle yield four different adducts resulting from endo or exo substitutions at the B6 or B9 borons (Figure 7). The relative energies of the **3-R** and **3′-R** structures and the **B-TS2** (17.7 kcal/mol) and **C-TS2** (21.8 kcal/mol) barriers clearly favor initial adduct formation at B6, but the formation of 9-*exo*-NH_3-6-*exo*-(C_3H_7)-$B_{10}H_{12}^-$ is thermodynamically favored.

Electrophilic $B_{10}H_{13}^-$ and 6-R-$B_{10}H_{12}^-$ Dehydrogenative Alkyne-Insertion Reactions. The first paper[1] in this series reported that, unlike reactions in conventional organic solvents where Lewis base catalysts are required, decaborane dehydrogenative alkyne-insertion reactions proceed rapidly in biphasic ionic-liquid/toluene mixtures at 120 °C with a wide variety of terminal and internal alkynes, thus providing efficient, one-step routes to functional *o*-carborane 1-R-1,2-$C_2B_{10}H_{11}$ and 1-R-2-R′-1,2-$C_2B_{10}H_{10}$ derivatives. The experimental data for these reactions along with the parallel studies of the reactions of $B_{10}H_{13}^-$ salts with alkynes supported the reaction sequence shown in Figure 8 involving: (1) the initial ionic-liquid promoted formation of the $B_{10}H_{13}^-$ anion, (2) addition of $B_{10}H_{13}^-$ to the alkyne to form an *arachno*-R,R′-$C_2B_{10}H_{13}^-$ anion, and (3) protonation of *arachno*-R,R′-$C_2B_{10}H_{13}^-$ to form the final neutral 1-R-2-R′-1,2-$C_2B_{10}H_{10}$ carborane with loss of hydrogen. As discussed in the following two sections, we have now computationally explored the pathways and intermediates involved in steps 2 and 3 for the reactions of both $B_{10}H_{13}^-$ and 6-(C_3H_7)-$B_{10}H_{12}^-$ with propyne.

(D) $B_{10}H_{13}^-$ Dehydrogenative Propyne-Insertion. The optimized structures and the relative MP2 energies are given in Figure 9 and Table 1. Selected geometrical parameters are given in Table 2.

The initial step in this reaction again involves the conversion of **1** to **3** by the process discussed earlier (Figure 3). Electrophilic attack by **3** at the HOMO propyne π-orbital through **D-TS2** (5.7 kcal/mol) then produces **D-Int3**. The C_a-C_b bond length in **D-TS2** (1.219 Å) is still that of a triple bond with the Me−C_a−C_b (176.8°) and C_a−C_b−H (170.9°) angles remaining near linear. But in **D-Int3**, the increase in the C_a-C_b length (1.277 Å) and the decreases in the Me−C_a−C_b (149.1°) and C_a−C_b−H (148.7°) angles, along with the shortening of the B6−C_a (1.672 Å) and B6−C_b

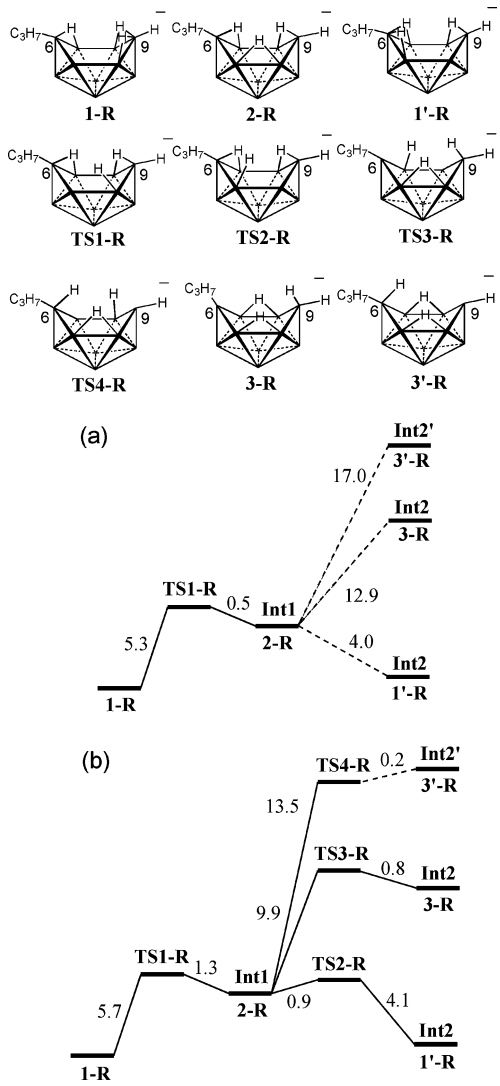

Figure 5. Possible pathways for the interconversions of the **1-R**, **1′-R**, **2-R**, **3-R**, and **3′-R** structures of 6-(C_3H_7)-$B_{10}H_{12}^-$. (a) Relative calculated energies (0 K) at the MP2 (6−311+G(d,p) level (HF/IRC calculations located transition states between the intermediates connected by the dashed lines, but they are not shown in the figure because the MP2 calculated energies of these transition states dropped below those of one of their connected intermediates) and (b) DFT (B3LYP/6−31+G(d,p)) free energies at 393.15 K (from Table S1, Supporting Information). All calculated energies are in kcal/mol.

(1.688 Å) lengths are consistent with the formation of a π-complex with donation to the LUMO orbital at the B6 boron. The formation of π-complex intermediates and transition-states with geometries similar to that of **D-Int3** have previously been computationally identified by McKee in his studies of the reactions of B_2H_6 and B_4H_8 with acetylene.[13] The **D-Int3** π-complex then converts to **D-Int4** via **D-TS3** with only a 0.4 kcal/mol barrier. In **D-TS3**, while maintaining the interaction with B6 (B6−C_a, 1.629 Å; B6−C_b, 1.729 Å), the propyne has rotated such that the B7−C_b length decreases to 2.246 Å and B5−C_a increases to 2.732 Å. This trend continues into **D-Int4**, where the observed B−C bond lengths (B7−C_b, 1.610 Å; B6−C_b, 2.310 Å; B6−C_a 1.551 Å, B5−C_a, 2.981 Å) and the

(13) (a) McKee, M. L. *J. Am. Chem. Soc.* **1995**, *117*, 8001–8009. (b) McKee, M. L. *J. Am. Chem. Soc.* **1996**, *118*, 421–428.

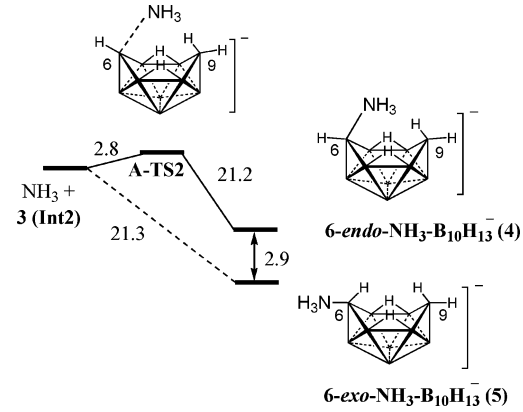

Figure 6. Possible pathways (**A**) for the formation of 6-*endo*- and 6-*exo*-NH_3-$B_{10}H_{13}^-$. The MP2 calculated energies are in kcal/mol. The dashed line indicates that the HF/IRC calculation located a transition state between (**3** + NH_3) and **5**, but it is not shown in the figure because the MP2 calculated energy of this transition state dropped below that of (**3** + NH_3).

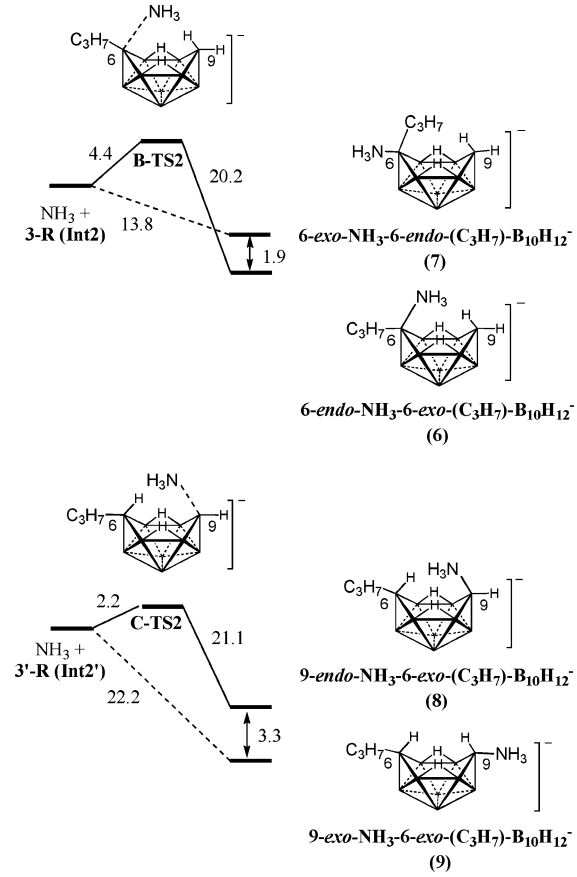

Figure 7. Possible pathways for the reaction of 6-(C_3H_7)-$B_{10}H_{12}^-$ with NH_3 at B6 (**B**) and B9 (**C**). The MP2 calculated energies are in kcal/mol. The dashed lines indicate that the HF/IRC calculations located transition states between both (**3** + NH_3) and **7** and (**3′-R** + NH_3) and **9**, but they are not shown in the figures because the MP2 calculated energies of these transition states dropped below those of (**3** + NH_3) and (**3′** + NH_3), respectively.

additional increase in the C_a−C_b length (1.349 Å) along with the decreases in the Me−C_a−C_b (126.3°) and C_a−C_b−H (121.2°) angles clearly indicate the formation of stronger bonding interactions between B6−C_a and B7−C_b. This change also forces the bridge-hydrogen at the B7−B8 edge in **D-TS3** to move to the B8−B9 edge in **D-Int4**. **D-Int5** is

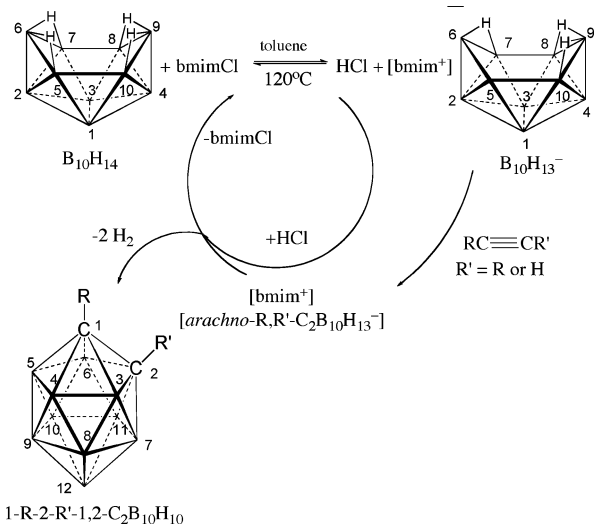

Figure 8. Proposed overall reaction scheme for ionic liquid promoted decaborane dehydrogenative alkyne-insertion.

then formed through **D-TS4** by a process involving the movement of the C_a carbon from its position near B6 to a position midway between B5 and B6. In **D-TS4**, the C_a-C_b distance only slightly lengthens (1.353 Å) and the B7−C_b (1.609 Å) and B6−C_a (1.550 Å) lengths are maintained, while the B5−C_a length (2.313 Å) decreases compared to its value in **D-Int4**. A frequency analysis confirmed that the **D-TS4** imaginary frequency is for the vibration between B5 and C_a. The formation of a bond with B5 is also consistent with the **D-Int4** charge analysis which showed B5 to be the most positively charged facial boron. To make room for the B5−C_a interaction, the B5−B10 bridging hydrogen in **D-Int4** moves to the endo-B10 position in **D-TS4**. The bond lengths in **D-Int5**, indicate that while B6 is still bound to both propyne carbons (B6−C_b, 1.657 Å; B6−C_a 1.722 Å), strong B7−C_b, (1.588 Å) and B5−C_a, (1.555 Å) interactions have been formed resulting in further elongation of the C_a-C_b bond to 1.425 Å.

Consistent with the computational results on the Lewis base adducts presented in the previous section, formation of *exo* propyne π-adduct **D-Int3′** was actually found to have a lower kinetic barrier than the *endo*-**D-Int3** adduct, but no forward pathway could be found leading from **D-Int3′** to alkyne-insertion. However, *exo*-**D-Int3′** can re-enter the reaction pathway with a backward 15.1 kcal/mol barrier from **D-Int3′** to **3** (**Int2**) + **propyne**.

To obtain the final neutral 1-methyl-*o*-carborane product, protonation of **D-Int5** is required. As discussed in the earlier paper,[1] for the $B_{10}H_{14}$/alkyne reactions in ionic liquids, protonation by the HCl originally generated by the ionic-liquid-promoted ionization of decaborane is likely. In the $[Et_3NH^+][B_{10}H_{13}^-]$/alkyne reactions, protonation by Et_3NH^+ with release of Et_3N and H_2 occurred. A computational investigation of the protonation of **D-Int5** by Et_3NH^+ could not locate a stable structure for a neutral *arachno*-R-$C_2B_{10}H_{15}$ carborane. However, protonation of **D-Int5** accompanied by loss of one equivalent of H_2 yielded the dehydrogenated intermediate **D-Int6**, which then proceeds to form the final 1-(CH_3)-1,2-$C_2B_{10}H_{11}$ product through **D-TS5**. In **D-Int6**, the

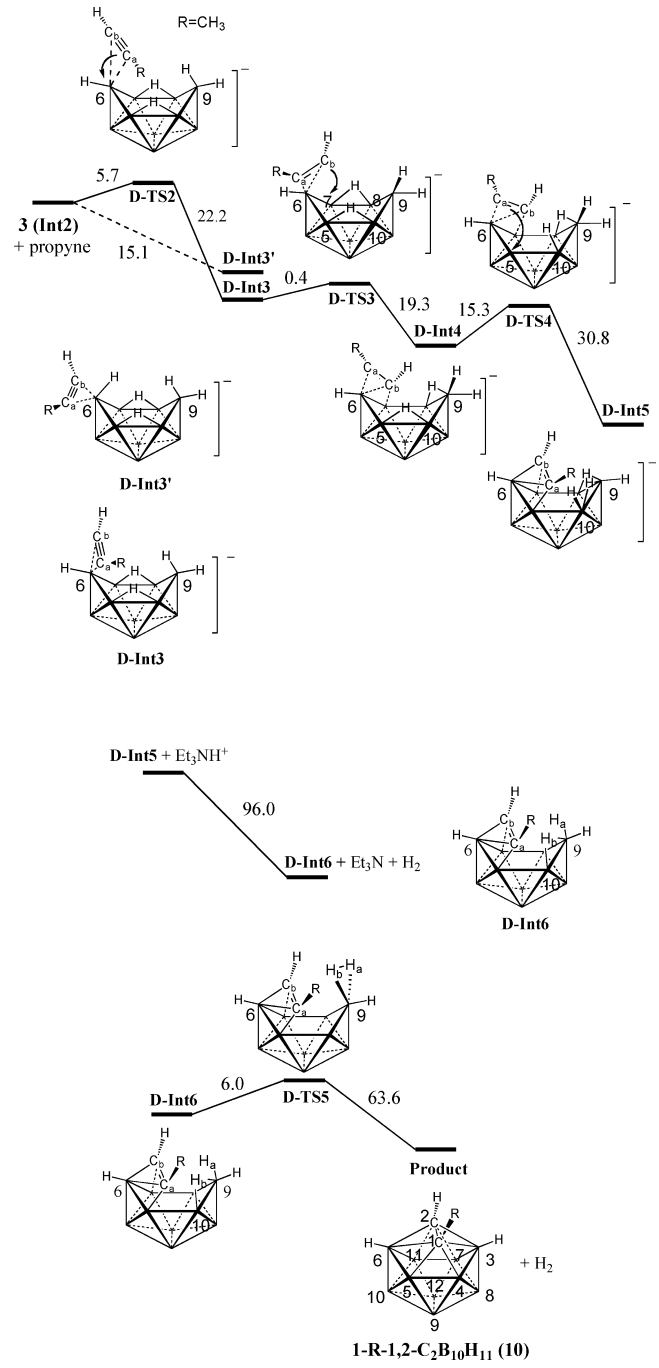

Figure 9. (**D**) A possible pathway for $B_{10}H_{13}^-$ electrophilic dehydrogenative propyne-insertion via structure **3**. The MP2 calculated energies are in kcal/mol. The dashed line indicates that the HF/IRC calculation located a transition state between (**3** + propyne) and **D-Int3′**, but it is not shown in the figure because the MP2 calculated energy of this transition state dropped below that of (**3** + propyne).

bridging-hydrogens, H_a and H_b, are 1.705 Å apart, but in **D-TS5**, the H_a-H_b distance is only 0.774 Å, and the **D-TS5** imaginary frequency, corresponding to a B9−H_2 (H_a-H_b) vibration orthogonal to B5−B10−B8-B7 plane, appears to be the prelude to hydrogen elimination. In the final step, elimination of these two hydrogens as H_2 and alkyne-insertion completes the reaction. The high exothermicity of the hydrogen elimination (63.6 kcal/mol) step combined with its favorable entropic contribution provides a strong thermodynamic driving force for this reaction.

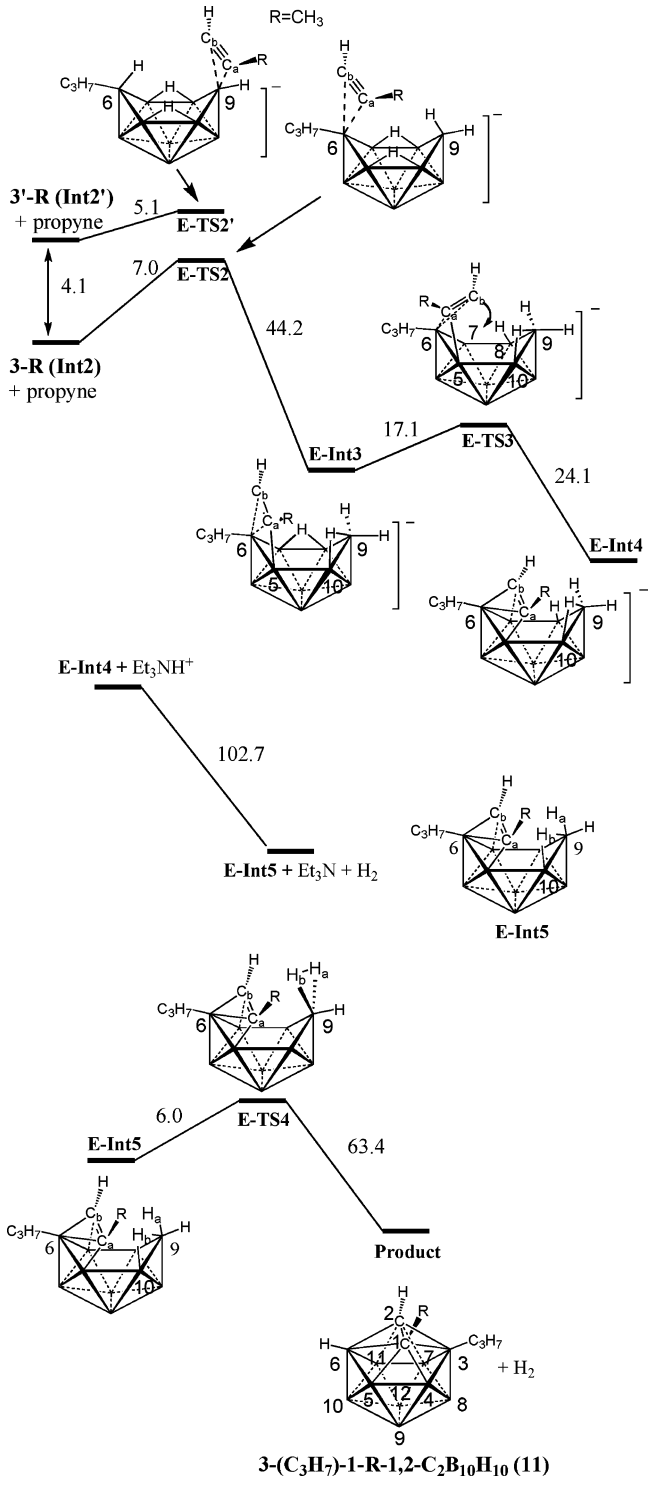

Figure 10. (**E**) A possible pathway for 6-(C_3H_7)-$B_{10}H_{12}^-$ electrophilic dehydrogenative propyne-insertion via structure **3-R**. The MP2 calculated energies are in kcal/mol.

(E) 6-(C_3H_7)-$B_{10}H_{12}^-$ Dehydrogenative Propyne-Insertion. The optimized structures and the relative MP2 energies are given in Figure 10 and Table 1. Selected geometrical parameters are given in Table 3.

As shown in Figure 10, the reaction with 6-(C_3H_7)-$B_{10}H_{12}^-$ proceeds in a manner similar to that of **3** and propyne, with the initial step involving the conversion of the ground-state structure **1-R** to the electrophilic structure **3-R** by the process (17.7 kcal/mol) depicted in Figure 5. Propyne binding at the

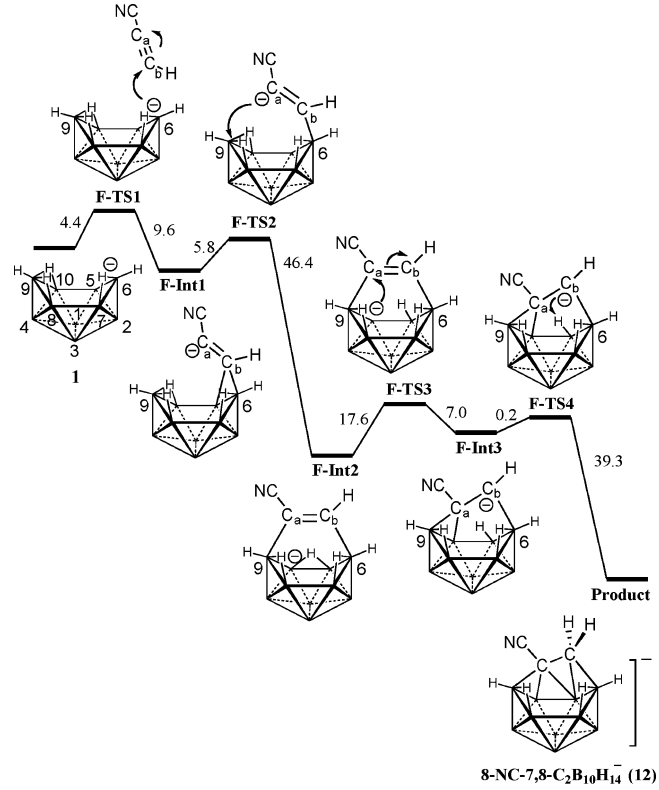

Figure 11. (**F**) A possible pathway for the nucleophilic reaction of $B_{10}H_{13}^-$ with cyanoacetylene via structure **1**. The MP2 calculated energies are in kcal/mol.

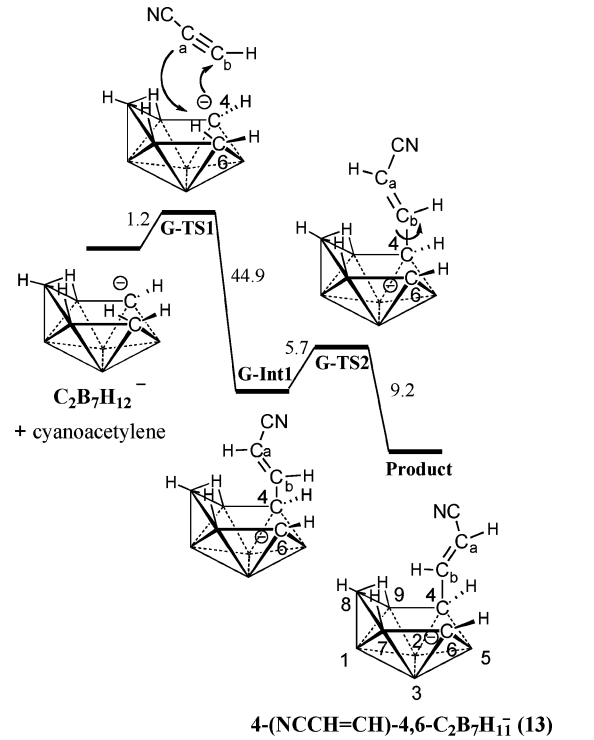

Figure 12. (**G**) A possible pathway for the nucleophilic reaction of 4,6-$C_2B_7H_{12}^-$ with cyanoacetylene. The MP2 calculated energies are in kcal/mol.

LUMO orbital localized on the B6 boron of **3-R** then occurs through a three-center type interaction (B6−C_a 2.513 Å; B6−C_b 2.213 Å) in **E-TS2** to give **E-Int3**. Propyne adduct formation through **E-TS2** at the B6-boron of **3-R** is clearly

more favorable than at the B9-boron of the higher energy **3-R′** and **E-TS2′** structures.

In **E-Int3**, C_a forms an additional bonding interaction with B5 (1.616 Å); the C_a-C_b bond lengthens (1.355 Å), and the C_a-C_b-H (121.9°) and C_b-C_a-Me (123.2°) angles decrease. Conversion of **E-Int3** to **E-Int4** through **E-TS3** then occurs by the formation of a C_b-B7 bond (1.598 Å) in **E-Int4** resulting in additional C_a-C_b bond lengthening (1.391 Å). Protonation of the **E-Int4** anion by Et_3NH^+ with loss of Et_3N and one equivalent of H_2 produces neutral **E-Int5**. Elimination of one bridging-hydrogen and the *endo*-B9-H of **E-Int5** through **E-TS4** then leads to the final observed product, 1-(CH_3)-3-(C_3H_7)-1,2-$C_2B_{10}H_{10}$. Again, the reaction is driven forward by the high exothermicity (63.4 kcal/mol) and entropically favorable hydrogen-elimination step.

(F) Nucleophilic Reaction of $B_{10}H_{13}^-$ with Cyanoacetylene. In contrast to the reactions discussed in the previous section which led to *o*-carborane formation, Su has previously shown[14] that cyanoacetylene readily reacts with $K^+B_{10}H_{13}^-$ at 0 °C to give the dicarbon inserted product, *arachno*-8-(NC)-7,8-$C_2B_{10}H_{14}^-$. As a result of the strong polarizing effect of the cyano group, the terminal carbon of cyanoacetylene has a partial positive charge and is activated for nucleophilic attack.[15] Thus, in contrast to the electrophilic reactions discussed in the previous section, Su proposed[14] that $B_{10}H_{13}^-$ is a nucleophile, directly attacking the terminal carbon to generate an anionic *σ*-bonded intermediate with the negative charge then becoming localized on the internal vinyl-carbon. This intermediate could then further react by formation of a new bond between the internal carbon and an electrophilic boron site on the cluster, resulting in cyclization at the internal carbon and dicarbon insertion with the terminal carbon being incorporated as a CH_2 fragment. As shown in Figure 11, our computational studies support this proposed scheme. The calculated energies and selected geometrical parameters are listed in Tables 1 and 4, respectively.

Consistent with the high electron density localized between the B5 and B6 atoms in the HOMO of structure **1** in Figure 1, the reaction proceeds by initial nucleophilic attack by **1** at the terminal cyanoacetylene carbon C_b through **F-TS1** to give **F-Int1**. The low initial barrier of only 4.4 kcal/mol is consistent with the fact that experimentally these reactions were found[14] to readily proceed at temperatures as low as 0 °C. In **F-TS1**, the terminal cyanoacetylene carbon is approaching the B5−B6 edge and although the B6−C distances are still long, $B6-C_b$ 1.944 Å and $B5-C_b$ 2.466 Å, the acetylenic C_a-C_b bond has lengthened from its 1.211 Å value in cyanoacetylene to 1.271 Å and the $H-C_b-C_a$ angle has decreased to 133.5° both indicating a rehybridization of the terminal carbon as it begins to accept electron density from the B5−B6 edge. In **F-Int1**, the terminal carbon has established strong interactions with both B5 and B6, $B6-C_b$ (1.724 Å) and $B5-C_b$ (1.704 Å), the C_a-C_b bond is elongated to 1.377 Å, and both the $C_b-C_a-C(N)$ (120.0°) and C_a-C_b-H (120.0°) angles are no longer linear.

F-Int2 is next formed via **F-TS2** by nucleophilic attack of the acetylenic anion at the B9 atom. In **F-TS2**, the terminal acetylenic carbon has moved away from B5 ($B5-C_b$, 2.462 Å) such that its primary interaction is with B6 ($B6-C_b$, 1.677 Å). The distance between B9 and the internal acetylenic carbon is still long ($B9-C_a$, 2.602 Å), but much shorter than in **F-Int1** ($B9-C_a$, 3.213 Å) and a frequency analysis confirmed that the **F-TS2** imaginary frequency results from the vibration between C_a and B9. A charge analysis also showed B9 to be more positive than either B8 or B10. To facilitate the $B9-C_a$ interaction, the B9−B10 bridging-hydrogen in **F-Int1** moves nearer the *endo*-B10 position in **F-TS2**. In **F-Int2**, the $B9-C_a$ (1.631 Å) and $B6-C_b$ (1.612 Å) lengths indicate strong bonding interactions as the cyanoacetylene has now been essentially converted to a cis-substituted olefin ($HC_b{=}C_a(CN)$, 1.359 Å) that is bridging the cage framework at the endo-positions of the B6 and B9 borons, with the three bridging hydrogens positioned as they are in the structure of **2**.

As **F-Int2** is converted to **F-Int3** via **F-TS3** a new $B10-C_a$ bond is formed. Thus, while the $B10-C_a$ distance is long (2.863 Å) in **F-Int2**, it starts to shorten in **F-TS3** (2.278 Å) then decreases to only 1.684 Å in **F-Int3**, while still maintaining a strong interaction with B9 (1.764 Å). In **F-Int3** the C_a carbon is bridging the B9−B10 edge with a $B9-C_a-B10$ angle of 64.5° that is near its value in the final product. It is also significant that the bridging hydrogen at the B5−B10 edge in **F-Int2** is converted to an *endo*-B5 position directed toward C_b in both **F-TS3** and **F-Int3**. In fact, the formation of the final product through **F-TS4** involves the transfer of this hydrogen to C_b and the formation of new B5 bonding interactions with both of the acetylenic carbons $B5-C_b$ and $B5-C_a$. The calculated distances for these bonds as well as for the elongation observed for the C_a-C_b bond (1.555 Å) in the final carborane product are in excellent agreement with the crystallographically determined structure[14] of this carborane.

(G) Nucleophilic Reaction of 4,6-$C_2B_7H_{12}^-$ with Cyanoacetylene. In a reaction related to that in the previous section, Su reported[14] that the 4,6-$C_2B_7H_{12}^-$ anion also reacts as a nucleophile toward cyanoacetylene. As in the $B_{10}H_{13}^-$ reaction, it was proposed that this reaction involved nucleophilic attack by the 4,6-$C_2B_7H_{12}^-$ anion at the terminal cyanoacetylene carbon with the olefinic anion abstracting the *endo*-proton at C6 to form 4-$(NCCH{=}CH)$-4,6-$C_2B_7H_{11}^-$. As illustrated in Figure 12, our computational analysis again supports this sequence with the initial nucleophilic attack of 4,6-$C_2B_7H_{12}^-$ at the terminal cyanoacetylene carbon via **G-TS1** to produce **G-Int1** with the low barrier (1.2 kcal/mol) again consistent with the experimentally observed low temperature reaction. In **G-TS1**, as the cyanoacetylene approaches C4 ($C4-C_b$, 1.994 Å), the C_a-C_b distance (1.257 Å) lengthens and the C_a-C_b-H (138.9°) angle decreases so that the cage *endo*-C6-H is pointed toward the C_a cy-

(14) (a) Su, K; Carroll, P. J.; Sneddon, L. G. *J. Am. Chem. Soc.* **1993**, *115*, 10004–10017. (b) Su, K; Barnum, B.; Carroll, P. J.; Sneddon, L. G. *J. Am. Chem. Soc.* **1992**, *114*, 2730–2731.

(15) (a) Bohlmann, F.; Bresinsky, E. *Chem. Ber.* **1964**, *97*, 2109–2117. (b) Dickstein, J. I.; Miller, S. I. In *The Chemistry of the Carbon−Carbon Triple Bond*; Patai, S., Ed.; Wiley: New York, 1978; Chapter 19, pp 813−955.

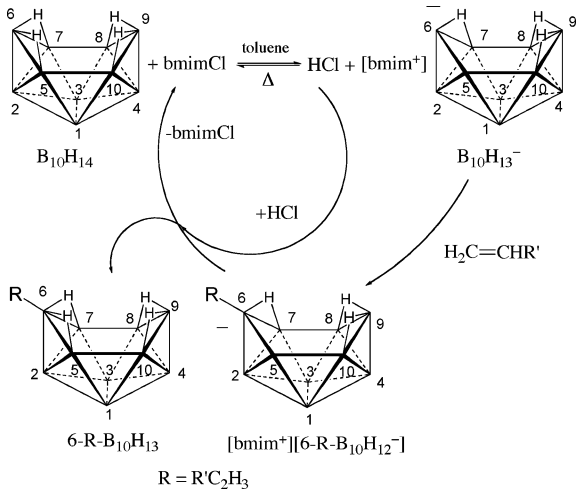

Figure 13. Proposed overall reaction scheme for ionic-liquid-promoted $B_{10}H_{14}$ olefin-hydroboration.

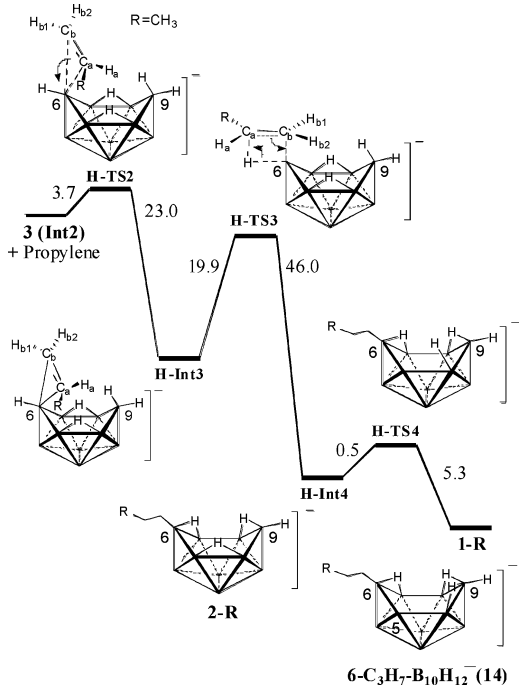

Figure 14. (**H**) A possible endo pathway for electrophilic $B_{10}H_{13}^-$ propylene-hydroboration via structure **3**. The MP2 calculated energies are in kcal/mol.

anoacetylene carbon. Transfer of this proton to C_a results in the formation of **G-Int1** where a C4−C_b bond (1.485 Å) has also been formed. The C_a−C_b bond length (1.356 Å) and H−C_b−C_a (115.8°) and C_b−C_a−C(N) (120.9°) angles indicate sp^2 geometry at the terminal carbon (Table 5). A rotation through **G-TS2** then converts **G-Int1** into the 4-(NCCH═CH)-4,6-$C_2B_7H_{11}^-$ final product.

(H) Electrophilic $B_{10}H_{13}^-$ Olefin-Hydroborations. The second paper in this series,[2] demonstrated that decaborane olefin-hydroboration reactions proceed in biphasic ionic-liquid/toluene mixtures with a wide variety of olefins to provide simple high-yield routes to 6-R-$B_{10}H_{13}$ derivatives with the experimental evidence again indicating that the $B_{10}H_{13}^-$ anion was the key reactant (Figure 13). As described below, DFT and IRC studies of the reaction $B_{10}H_{13}^-$ with propylene led to the two pathways illustrated in Figures 14

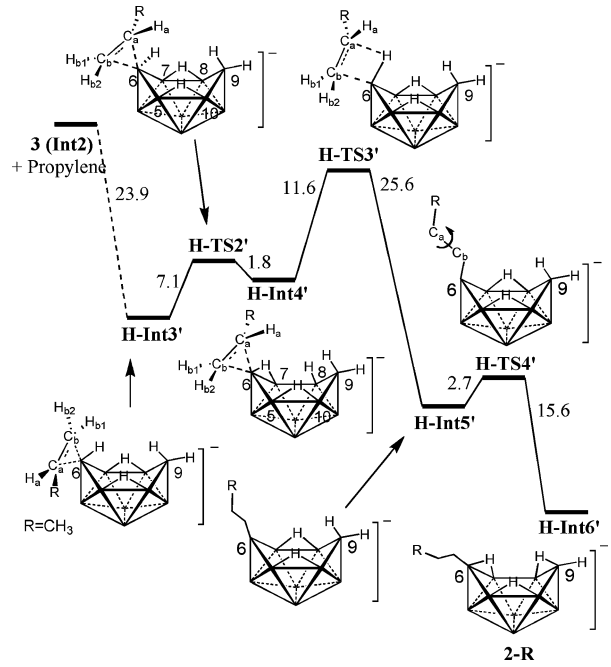

Figure 15. (**H**) A possible exo pathway for electrophilic $B_{10}H_{13}^-$ propylene-hydroboration via structure **3**. The MP2 calculated energies are in kcal/mol. The dashed line indicates that the HF/IRC calculation located a transition state between (**3** + propylene) and **H-Int3′**, but it is not shown in the Figure because the MP2 calculated energy of this transition state dropped below that of (**3** + propylene).

and Figure 15, corresponding to initial olefin binding at the B6 endo and exo positions, respectively. Selected geometrical parameters are listed in Tables 6 and 7.

Both pathways again start with the conversion of **1** to **3** by the process shown in Figure 3. An endo approach of the olefin (Figure 14) at **3** then leads to **H-Int3** through **H-TS2**. In **H-TS2**, the B6−H bond is nearly perpendicular (86.0° H−B6−C_b−C_a dihedral angle) to the C_a−C_b double bond and the B6−C_a (2.504 Å) and B6−C_b (2.393Å) lengths and B6−C_a−C_b and B6−C_b−C_a angles (69.5 and 78.5°) indicate a 3-center distorted triangular arrangement. The long (B6)H−C_a (2.641 Å) and (B6)H−C_b (2.566 Å) lengths indicate little interaction between the B6−H and the carbons. The C_a−C_b double bond (1.355 Å) length and the sum of the angles around C_a (359.8°) and C_b (359.6°) indicate no olefin rehybridization. In **H-Int3**, the C_a−B6 (1.737 Å) and C_b−B6 (1.715 Å) lengths decrease, and the C_a−C_b bond (1.443Å) elongates, consistent with the formation of a 3-center or π-type complex where electron density from the olefin is donated to the borane LUMO orbital localized at B6. The 97.0° H−B6−C_b−C_a dihedral angle and the long (B6)H−C_a (2.356 Å) and (B6)H−C_b (2.342 Å) distances indicate little interaction between B6−H and the carbons. The initial formation of the π-complex **H-Int3** via the three-centered **H-TS2** is again consistent with similar intermediates and/or transition states computationally identified in earlier studies of ethylene-hydroboration by B_4H_{10} and R_2BH.[16]

H-Int3 then converts to **H-Int4** via **H-TS3** by a process involving rotation of the olefin to a position where the C_a−C_b

(16) (a) Bühl, M; McKee, M. L. *Inorg. Chem.* **1998**, *37*, 4953–4958. (b) Hommes, N. J. R. v. E.; Schleyer, P. v. R. *J. Org. Chem.* **1991**, *56*, 4074–4076.

Table 2. Selected Distances (Å) and Angles (deg) for the Reaction (**D**) of $B_{10}H_{13}^-$ with Propyne via Structure **3**

	D-TS2	D-Int3	D-TS3	D-Int4	D-TS4	D-Int5	D-Int6	D-TS5
C_a-C_b	1.219	1.277	1.284	1.349	1.353	1.425	1.472	1.531
C_a−B6	2.423	1.672	1.629	1.551	1.550	1.722	1.698	1.718
C_a−B5	3.138	2.629	2.732	2.981	2.313	1.555	1.610	1.662
C_b−B6	2.319	1.688	1.729	2.310	2.005	1.657	1.693	1.702
C_b−B7	3.087	2.458	2.246	1.610	1.609	1.588	1.649	1.654
B5−B10	1.903	1.841	1.830	1.783	1.902	3.021	1.892	1.836
B7−B8	1.911	1.848	1.873	2.002	2.104	1.979	1.842	1.834
H_a-H_b						1.886	1.705	0.774
C_a-C_b−H	170.9	148.7	146.6	121.2	119.8	120.7	117.3	116.7
C_b-C_a−Me	176.8	149.1	146.5	126.3	130.7	120.7	119.8	118.7

Table 3. Selected Distances (Å) and Angles (deg) for the Reaction (**E**) of 6-R-$B_{10}H_{12}^-$ with Propyne via Structure **3-R**

	E-TS2	E-Int3	E-TS3	E-Int4	E-Int5	E-TS4
C_a-C_b	1.221	1.355	1.361	1.391	1.471	1.531
C_a−B6	2.513	2.378	2.150	1.740	1.721	1.743
C_a−B5	3.213	1.616	1.616	1.612	1.604	1.653
C_b−B6	2.213	1.542	1.548	1.714	1.709	1.718
C_b−B7	2.920	2.988	2.232	1.598	1.643	1.646
B5−B10	1.917	1.971	2.085	2.086	1.895	1.837
B7−B8	1.906	1.780	1.895	2.109	1.839	1.830
H_a-H_b					1.705	0.774
C_a-C_b−H	165.9	121.9	126.0	119.9	117.4	116.8
C_b-C_a−Me	176.7	123.2	122.4	122.5	119.9	119.4

Table 4. Selected Distances (Å) and Angles (deg) for the Reaction (**F**) of $B_{10}H_{13}^-$ with Cyanoacetylene via Structure **1**

	F-TS1	F-Int1	F-TS2	F-Int2	F-TS3	F-Int3	F-TS4	product	X-ray[10]
C_a-C_b	1.271	1.377	1.326	1.359	1.367	1.397	1.448	1.555	1.504(9)
C_b−C(N)	1.351	1.401	1.386	1.432	1.435	1.444	1.440	1.443	1.455(7)
C≡N	1.183	1.179	1.178	1.169	1.168	1.166	1.167	1.167	1.144(7)
B6−C_b	1.944	1.724	1.677	1.612	1.586	1.564	1.563	1.626	1.579(9)
B5−C_b	2.466	1.704	2.462	2.839	2.835	2.755	2.203	2.328	2.173(9)
B9−C_a	3.399	3.213	2.602	1.631	1.635	1.764	1.718	1.650	1.649(7)
B10−C_a	3.616	3.192	3.173	2.863	2.278	1.684	1.623	1.690	1.657(8)
C_b-C_a−C(N)	174.1	120.0	132.3	119.3	118.8	116.3	114.4	110.6	108.8(3)
C_a-C_b−H	133.5	120.0	122.8	118.5	116.4	115.1	115.3		
B9−C_a-C_b				123.4	125.0	118.7	121.5	117.4	118.6(3)
B6−C_b-C_a				124.3	126.7	128.0	128.4	110.4	112.4(3)
B9−C_a−B10				50.6	58.4	64.5	66.7	67.8	66.5(3)

Table 5. Selected Distances (Å) and Angles (deg) for the Reaction (**G**) of 4,6-$C_2B_7H_{12}^-$ with Cyanoacetylene

	G-TS1	G-Int1	G-TS2	product
C_a-C_b	1.257	1.356	1.349	1.362
C_b-C_a	1.355	1.423	1.427	1.421
C≡N	1.180	1.169	1.168	1.170
C4−C_b	1.994	1.485	1.507	1.468
H−C_b-C_a	138.9	115.8	116.5	118.5
C_b-C_a−C(N)	176.3	120.9	122.1	123.1

Table 6. Selected Distances (Å) and Angles (deg) for the Reaction (**H**) of $B_{10}H_{13}^-$ with Propylene via the *endo*-B6 Position of Structure **3**

	H-TS2	H-Int3	H-TS3	H-Int4	H-TS4
C_a-C_b	1.355	1.443	1.439	1.540	1.539
C_a−B6	2.504	1.737	1.796		
C_b−B6	2.393	1.715	1.665	1.602	1.607
R−C_a-H_a		116.5	113.8	115.0	
$H_a-C_a-C_b$		117.8	114.3	117.6	
R−C_a-C_b		125.5	122.9	122.2	
$H_{b1}-C_b-H_{b2}$		117.5	114.6	114.2	
$H_{b1}-C_b-C_a$		121.6	119.6	117.6	
$H_{b2}-C_b-C_a$		120.5	117.7	118.4	
$C_a-C_b-B_6$		78.5	66.1	70.3	
$C_b-C_a-B_6$		69.5	64.5		
C_a−B6−C_b		32.0	49.4		
C_b-B_6−H		84.5	105.7	107.3	
C_a−H−B6				72.1	
C_b-C_a−H				94.4	
H−B6−C_b-C_a		86.0	97.0	36.4	

bond is more aligned with the B6−H bond axis (36.4° H−B6−C_b-C_a dihedral angle). In **H-TS3**, B6 is much closer to C_b (1.665 Å) than to C_a (1.796 Å) and (B6)H is closer to C_a (1.742 Å) than to C_b (2.343 Å), consistent with the 4-center geometry needed for olefin-hydroboration. **H-TS3** then converts to the hydroborated intermediate 6-(C_3H_7)-$B_{10}H_{12}^-$, **H-Int4** (**2-R**) by the addition of the B6−H across the propylene C_a-C_b bond to form the saturated propyl-substituent at B6 (C_a-C_b, 1.540 Å; B6−C_b, 1.602 Å). The B5−B10 bridging hydrogen in **H-Int4** then moves to an endo-B10 position in **H-TS4** on its way to the B9−B10 edge in the 6-(C_3H_7)-$B_{10}H_{12}^-$ product.

An exo approach of the propylene (Figure 15) at **3** proceeds with a low barrier to **H-Int3′**. Consistent with the calculations on the $B_{10}H_{13}^-/NH_3$ reactions discussed earlier (Figure 6), formation of the exo-adduct intermediate **H-Int3′** is both kinetically and thermodynamically favored over the endo-adduct **H-Int3** (Figure 14). At **H-Int3′**, the shortened B6−C_a (1.759 Å) and B6−C_b (1.732 Å) lengths and the elongated C_a-C_b bond (1.419Å) are similar to those in **H-Int3**, again suggesting the formation of a 3-center or π-type complex where electron density from the olefin is

Table 7. Selected Distances (Å) and Angles (deg) for the Reaction (**H**) of $B_{10}H_{13}^-$ with Propylene via the *exo*-B6 Position of Structure **3**

	H-Int3′	**H-TS2′**	**H-Int4′**	**H-TS3′**
C_a-C_b	1.419	1.453	1.486	1.454
C_a-B6	1.759	1.697	1.642	1.779
C_b-B6	1.732	1.656	1.611	1.628
B6−H	1.192	1.210	1.282	1.232
$R-C_a-H_a$	115.4	114.1	113.3	114.7
$H_a-C_a-C_b$	117.1	116.6	116.2	118.0
$R-C_a-C_b$	122.8	122.4	120.8	121.1
$H_{b1}-C_b-H_{b2}$	115.7	114.9	114.0	114.8
$H_{b1}-C_b-C_a$	119.9	118.3	117.5	117.4
$H_{b2}-C_b-C_a$	120.3	119.3	118.9	117.2
$C_a-C_b-B_6$	67.0	65.8	63.9	70.3
$C_b-C_a-B_6$	65.0	62.8	61.7	
C_a-B6-C_b	48.0	51.4	54.4	
C_b-B_6-H	109.6	113.3	111.1	106.5
C_a-H-B6				76.0
C_b-C_a-H				97.1
$H-B6-C_a-C_b$	80.3	70.7	71.2	30.1

donated to the borane LUMO orbital localized at B6. At this point, the B6−H bond is still nearly perpendicular to the C_a-C_b bond (80.3° $H-B6-C_a-C_b$ dihedral angle). **H-Int3′** then converts to **H-Int4′** via **H-TS2′**, where the propylene slightly rotates parallel to the B6−B9−B4-B2 plane (70.7°, $H-B6-C_a-C_b$ dihedral angle) and B6−H skews toward B7, with the imaginary frequency of **H-TS2′** corresponding to this rotation.

H-Int4′ then converts to **H-TS3′** with further bridge-hydrogen reorganization and olefin-rotation to bring the B6−H bond axis more aligned with C_a-C_b (30.1°, $H-B6-C_a-C_b$ dihedral angle). In **H-TS3′**, B6 is closer to C_b (1.628 Å) than to C_a (1.779 Å) and (B6)−H is much closer to C_a (1.616 Å) than to C_b (2.304 Å), again consistent with a 4-center-like geometry needed for olefin hydroboration. **H-TS3′** then converts to the hydroborated intermediate 6-(C_3H_7)-$B_{10}H_{12}^-$, **H-Int5′**, by addition of B6−H across C_a-C_b. **H-Int5′** converts to **H-Int6′** (**2-R**) via **H-TS4′** where the $R-C_a$ group rotates around C_b. The final conversion of **2-R** to **1-R** is the same as discussed in the endo hydroboration pathway (Figure 14).

The final products experimentally observed in both the decaborane olefin-hydroboration reactions carried out in ionic liquids and the reactions of the $[Et_3NH^+][B_{10}H_{13}^-]$ salt with olefins are the neutral 6-R-$B_{10}H_{13}$ compounds. Therefore, the last step in both cases must involve protonation of the 6-R-$B_{10}H_{12}^-$ anions. As discussed in the earlier paper,[2] for the $B_{10}H_{14}$/olefin reactions in the bmimCl ionic-liquid, protonation by the HCl originally generated in the ionic-liquid-promoted ionization of decaborane is likely, while in the $[Et_3NH^+][B_{10}H_{13}^-]$/olefin reactions, protonation by Et_3NH^+ with release of Et_3N occurs. This sequence is likewise consistent with the protonation observed in the dehydrogenative alkyne-insertion reaction discussed earlier.

In summary, the computational and experimental studies presented in this and the two preceding papers all indicate that the $B_{10}H_{13}^-$ anion is unique in its ability to function, depending upon the reactant and reaction conditions, as either a nucleophile or electrophile. Furthermore, the computational studies provide additional strong support for a reaction mechanism involving both the formation of $B_{10}H_{13}^-$ and its rearrangement to an electrophilic form as the key steps that lead to the reactivities observed in the ionic-liquid-promoted decaborane dehydrogenative alkyne-insertion and olefin-hydroboration reactions.

Acknowledgment. We thank the National Science Foundation for the support of this project. We also thank Professor David Dixon at the University of Alabama for his helpful comments.

Supporting Information Available: Table of B3LYP/6−31+G(d,p) level electronic and free energies at 0 and 393.15 K and tables listing Cartesian coordinates for optimized geometries. This material is available free of charge via the Internet at http://pubs.acs.org.

IC8010019